Cronfa - Swansea University Open Access Repository

This is an author produced version of a paper published in:
ACS Applied Nano Materials

Cronfa URL for this paper:
http://cronfa.swan.ac.uk/Record/cronfa50533

Paper:
Deng, S., Li, L. & Rees, P. (2019). Graphene/MoXY Heterostructures Adjusted by Interlayer Distance, External Electric Field and Strain for Tunable Devices. *ACS Applied Nano Materials*
http://dx.doi.org/10.1021/acsanm.9b00871

This item is brought to you by Swansea University. Any person downloading material is agreeing to abide by the terms of the repository licence. Copies of full text items may be used or reproduced in any format or medium, without prior permission for personal research or study, educational or non-commercial purposes only. The copyright for any work remains with the original author unless otherwise specified. The full-text must not be sold in any format or medium without the formal permission of the copyright holder.

Permission for multiple reproductions should be obtained from the original author.

Authors are personally responsible for adhering to copyright and publisher restrictions when uploading content to the repository.

http://www.swansea.ac.uk/library/researchsupport/ris-support/

ACS APPLIED NANO MATERIALS

Subscriber access provided by SWANSEA UNIV

Article

Graphene/MoXY Heterostructures Adjusted by Interlayer Distance, External Electric Field and Strain for Tunable Devices

Shuo Deng, Lijie Li, and Paul Rees

ACS Appl. Nano Mater., **Just Accepted Manuscript** • DOI: 10.1021/acsanm.9b00871 • Publication Date (Web): 24 May 2019

Downloaded from http://pubs.acs.org on May 28, 2019

Just Accepted

"Just Accepted" manuscripts have been peer-reviewed and accepted for publication. They are posted online prior to technical editing, formatting for publication and author proofing. The American Chemical Society provides "Just Accepted" as a service to the research community to expedite the dissemination of scientific material as soon as possible after acceptance. "Just Accepted" manuscripts appear in full in PDF format accompanied by an HTML abstract. "Just Accepted" manuscripts have been fully peer reviewed, but should not be considered the official version of record. They are citable by the Digital Object Identifier (DOI®). "Just Accepted" is an optional service offered to authors. Therefore, the "Just Accepted" Web site may not include all articles that will be published in the journal. After a manuscript is technically edited and formatted, it will be removed from the "Just Accepted" Web site and published as an ASAP article. Note that technical editing may introduce minor changes to the manuscript text and/or graphics which could affect content, and all legal disclaimers and ethical guidelines that apply to the journal pertain. ACS cannot be held responsible for errors or consequences arising from the use of information contained in these "Just Accepted" manuscripts.

is published by the American Chemical Society. 1155 Sixteenth Street N.W., Washington, DC 20036

Published by American Chemical Society. Copyright © American Chemical Society. However, no copyright claim is made to original U.S. Government works, or works produced by employees of any Commonwealth realm Crown government in the course of their duties.

1
2
3
4
5
6
7
8
9
10
11
12
13
14
15
16
17
18
19
20
21
22
23
24
25
26
27
28
29
30
31
32
33
34
35
36
37
38
39
40
41
42
43
44
45
46
47
48
49
50
51
52
53
54
55
56
57
58
59
60

Graphene/MoXY Heterostructures Adjusted by Interlayer Distance, External Electric Field and Strain for Tunable Devices

Shuo Deng[†‡], Lijie Li[*‡] and Paul Rees[*‡]
[†]Wuhan University of Technology, Wuhan 430070, China
[‡]College of Engineering, Swansea University, Swansea SA1 8EN, UK
[*]Emails: L.Li@swansea.ac.uk; P.Rees@swansea.ac.uk

ABSTRACT

Graphene has shown great promise in many electronic devices and systems since it was discovered. However doping control limits its use in devices. For addressing this problem, graphene/MoXY (X/Y=S, Se, Te and X ≠ Y) heterostructures have been investigated in this work. We analyze electronic and optical properties of the graphene/MoXY heterostructures under various effects such as interlayer distance, external electric field and mechanical strain by the first principles method. We find that interlayer distance and external electric field are two prominent parameters to induce tunable homogeneous doping of graphene (G). Compared with interlayer distance modulation, the tuning range of the carrier density in the graphene layer by the external electric field is wider. In the graphene/MoXY heterostructures, the highest carrier density of graphene is simulated to be $4.62 \times 10^{13}/cm^2$ for the G/TeMoS stacking under the electric field strength of 1.0V/ Å. The doping concentration of the graphene layer can be tuned from $3.94 \times 10^{13}/cm^2$ (hole) to $2.00 \times 10^{13}/cm^2$ (electron) subject to the external electric fields of -1.0V/ Å and 1.0V/ Å for the G/SMoTe type. In addition, the optical absorption coefficient of the heterostructure graphene/MoSSe is higher than 10^5/cm in the wavelength range from 550 nm to 800 nm. The results indicate that these graphene/MoXY heterostructures will have great applications in tunable nanoelectronic devices.

KEYWORDS: Graphene/MoXY heterostructure, Electronic property, Optical property, Interlayer distance, External electric field, Mechanical strain

1. INTRODUCTION

Since graphene was discovered as a promising 2-dimensional (2D) material in 2004[1], many extraordinary physical and chemical properties of graphene have been discovered, such as high electrical conductivity and carrier mobility[2-6], high thermal conductivity[7], and superior mechanical properties[8-9]. However, its applications in field-effect transistors (FETs) devices are limited because it does not have a bandgap due to the Dirac cone effect [10]. In this context, many other 2D materials with a bandgap were discovered and explored like hexagonal boron

1
2
3
4
5
6
7
8
9
10
11
12
13
14
15
16
17
18
19
20
21
22
23
24
25
26
27
28
29
30
31
32
33
34
35
36
37
38
39
40
41
42
43
44
45
46
47
48
49
50
51
52
53
54
55
56
57
58
59
60

nitride (h-BN) [11-12], transition metal dichalcogenides (TMDs) [13-15] and phosphorene (BP) [16-17]. In order for 2D materials to have even better physical and chemical properties for their use in transistor/sensor devices, changing the planner symmetry of TMDs can be a very effective approach, such as constructing MoSSe – Janus TMDs [18]. The monolayer MoSSe can be fabricated by fully replacing one side S with Se atoms using the chemical vapour deposition (CVD) [18]. Compared with traditional monolayer MoS_2, monolayer MoSSe has a stronger stability in structure asymmetry [19] due to the replacement of one of the S atoms with Se atom within the MoS_2 monolayer, which bring a larger intrinsic dipole[18, 20] and piezoelectricity [21] properties. Relevant applications for the Janus TMDs include the solar water splitting [22-24], bandgap engineering [25], optoelectronic devices [26-27] and natural doping [28].

In parallel with the investigation on novel 2D materials, the research of 2D materials based on van der waals (vdW) heterostructures has also been investigated theoretically and experimentally. In particular, graphene can build weak interlayer coupling with other 2D materials because it lacks of interlayer dangling bonds, such as graphene/h-BN [29-31], graphene/MoS_2 [32-37], graphene/BN [38-39], and graphene/GaSe heterostructures [40]. Graphene based vdW heterostructures show some new optoelectronic properties far beyond the isolated 2D materials, and keep the intrinsic electronic properties of individual 2D materials without degradation. More recently, the electronic properties of graphene/MoSSe heterostructures were researched. In 2017, two research groups reported that the Schottky barrier between graphene layer and MoSSe layer can be effectively modulated by interlayer distance and external electric field [41-42]. This finding demonstrated that the graphene/MoSSe heterostructures can be used to design high performance FETs. Mattias *et al* reported that Graphene/MoSSe/graphene trimorphic type can cause a high doping in graphene and build cross plane *pn*-junctions [28]. Interestingly, when graphene acting as electrodes and MoSSe being the transport channel, the photocurrent of the graphene/MoSSe/graphene device is larger than that of the corresponding silicon device, which illustrates that graphene/MoSSe/graphene stacking has a great potential as photovoltaic devices. Although there have been few theoretical efforts reported on the interlayer Schottky barrier and photocurrent curve of graphene-MoSSe structure, the influence of the interlayer distance, electric field and strain on the doping of graphene and optical properties of graphene/MoXY heterostructures have not been fully understood, especially for graphene/MoSTe and graphene/MoSeTe heterostructures.

In this work, we analyze electronic and optical properties of graphene/MoXY heterostructures in terms of the interlayer distance, external electric field and strain using the first principle method. The first principles method has been widely employed tools for investigating heterostructures and their derivatives [28, 41-45]. The Graphene/MoXY heterostructures can be obtained experimentally by the epitaxial growth or mechanical stacking. Annealing method, field-effect transistor devices and flexible substrates can be used to vary the interlayer distance, apply external electric field and strains on the heterostructures[46-48]. Although several research groups have theoretically analyzed the electric properties of the graphene/MoSSe heterostructure, there is a lack of work on the graphene/MoSTe and graphene/MoSeTe types, especially on their optical properties. Our results show that the interlayer distance and external electric field are two prominent factors

to change doping of graphene in the graphene/MoXY heterostructures. Compared with the interlayer distance modulation, external electric field can induce wider tuneability on the carrier density. For the graphene/MoXY heterostructures, the calculated highest carrier density of graphene can be $4.62 \times 10^{13}/cm^2$ for G/TeMoS stacking under 1.0V/ Å electric field strength. In additional, compared with the pristine monolayer MoSSe, the optical absorption coefficient is enhanced for the graphene/MoSSe within the wavelength range from 550 nm to 800 nm and absorption intensity is higher than10^5/cm. It is also found that the optical absorption spectrum of the graphene/MoSSe can be modulated by the interlayer distance, external electric field and strain. Adjustable carrier density under strain could lead to realization of novel strain gated transistors. Superior optical absorption coefficients of these heterostructures make them promising candidates in photovoltaic applications.

2. COMPUTATIONAL PROCEDURE

In the present model, the *ab initio* simulations are performed using the density functional theory (DFT) with the Linear Combination of Atomic Orbitals (LCAO) method as implemented in the Quantum Atomistix ToolKit (ATK2018) simulation tools [49]. In the structure optimization, the exchange-correlation functional chooses the generalized gradient approximation (GGA) with the parametrization of Perdew-Burke-Ernzerhof (PBE). For the van der Waals (vdW) interaction in the graphene/MoXY interface , we use the semi-empirical corrections by Grimme DFT-D2 model, which takes account the long-range vdW interaction [50]. In addition, the structure is fully relaxed until the force on each atom becomes smaller than 0.01 eV/Å, and the stress error tolerance is 0.001 eV/ Å^3. The cut-off energy of 500 eV and 20×20×1 k-points grid were used in the Brillouin zone. To avoid the interaction of the periodic boundary conditions, a large vacuum spacing of at least 25 Å is added along the *x*-direction. We examine the stability of the constructed Graphene/MoXY heterostructures by Born-Oppenheimer molecular dynamics (BOMD) simulation in ATK[51]. In the NVT Nose Hoover scheme, we set temperature at 450 K and the simulation has run through 3 ps thermostat timescale with 1 fs time step. After the BOMD simulation, only small changes appear in the Graphene/MoXY interior structure, which demonstrates a good thermal stability for Graphene/MoXY heterostructures. The GGA-PBE method usually underestimates the bandgap. The Heyd-Scuseria-Ernzerhof (HSE) and GW methods (it is approximated that the self-energy is the product of the single-particle Green function *G* and the screened interaction *W*) are two advanced methods in the electrical and optical properties simulation [52]. However, previous research show that GW method often estimates a higher bandgap than HSE method in TMDs [52]. For example, HSE and GW bandgaps of the monolayer MoS_2 are 2.04 eV and 2.53 eV, while the experiment result is about 1.80 eV [13]. In our paper, we used the HSE method, which often leads to an accurate simulation for the bandgap and lower computationally expensive than GW method [53]. In the optical absorption simulation, the absorption coefficient (α_a) can be calculated by [54]:

$$\alpha_a = \frac{2\omega}{c}\sqrt{\frac{\sqrt{\epsilon_1^2 + \epsilon_2^2} - \epsilon_1}{2}} \qquad (1)$$

Where c, ω, ϵ_1 and ϵ_2 are speed of light, angular frequency of light, real and imaginary parts of complex dielectric constant, respectively.

1 2 3 4 5 6 7 8 9 10 11 12 13 14 15 16 17 18 19 20 21 22 23 24 25 26 27 28 29 30 31 32 33 34 35 36 37 38 39 40 41 42 43 44 45 46 47 48 49 50 51 52 53 54 55 56 57 58 59 60

3. RESULTS AND DISCUSSION

3.1. Crystal structure and electronic properties of monolayer MoXY

As shown in Figure 1(a) and (b), to construct the models of graphene/MoXY heterostructures, we first optimized the lattice parameters of the individual monolayer MoSSe, MoSTe and MoSeTe. For the monolayer MoSSe, the optimized lattice parameters are a=b=3.25 Å. The distance between S and Se atom is 3.23 Å and the angle between the Mo-S and Mo-Se bonds is 81.4^{o}, which is consistent with the prior experimentally results [18]. For the monolayer MoSTe, the lattice parameters are a=b=3.36 Å and the distance between S and Te atom is 3.37 Å and the angle between the Mo-S and Mo-Te bonds is 81.6^{o}, which agrees well with previous reported [22, 55]. For the monolayer MoSeTe, the lattice parameters, distance from Se to Te atom and the angle between the Mo-Se and Mo-Te bonds are a=3.43 Å, b=3.48 Å and 82.4^{o}, which are also consistent with the theoretically reported by other groups [22, 55].

Figure 1(c) to (e) show the band structures of the Brillouin zone of high symmetry points along the path through *Γ-M-K-Γ* and the projected density of state (PDOS) of monolayer MoXY cells. Obviously, monolayer MoSSe and monolayer MoSeTe are direct bandgap semiconductor with bandgap value of 2.03 eV and 1.70 eV respectively. However, monolayer MoSTe is an indirect bandgap semiconductor with 1.48 eV bandgap. Calculation results show that the conduction band minimum (CBM) and valence band maximum (VBM) of monolayer MoSSe and monolayer MoSeTe are located at the *K* point in the Brillouin zone. While for monolayer MoSTe, the CBM is at the *K* point and the VBM is at the *Γ* point. Moreover, as shown in the PDOS of monolayer MoXY, the PDOS of CBM and VBM of monolayer MoXY are contributed mainly from the Mo-*d* orbital. This result is consistent with prior research[56]. Interestingly, the monolayer MoXY has an asymmetric structure, which leads to the charge redistribution and an intrinsic dipole on the surface, inducing an internal electric field from Y atom to X atom. Taking monolayer MoSSe as an example. An electrostatic potential difference ($\Delta\phi$) about 0.77 eV is formed between Se atom layer and S atom layer because the Se atom layer has a smaller electronegativity (positively charged) and the S atom layer has a larger electronegativity (negatively charged). The electrostatic potential difference of monolayer MoSTe and monolayer MoSeTe are 1.63 eV and 0.97 eV, respectively (Table 1). We can conclude that $\Delta\phi_{MoSTe}$>$\Delta\phi_{MoSeTe}$>$\Delta\phi_{MoSSe}$, which indicates that the monolayer MoSTe has the strongest intrinsic dipole and internal electric field in the monolayer MoXY. The main lattice parameters, bandgap, electrostatic potential difference, ionization potential and electron affinity are summarized in Table 1. As shown in the Figure 1(f), we calculated the optical absorption coefficient of monolayer MoXY within the wavelength range from 300 nm to 1600 nm. The monolayer MoXY exhibits a high absorption coefficient ($>1 \times 10^5$/cm) spectra from the ultraviolet region (300 nm) to the near infrared region (800 nm). Remarkably, the optical absorption coefficient of monolayer MoSTe and monolayer MoSeTe are higher than the monolayer MoSSe when the wavelength is longer than about 500 nm.

ACS Paragon Plus Environment

1
2
3
4
5
6
7
8
9
10
11
12
13
14
15
16
17
18
19
20
21
22
23
24
25
26
27
28
29
30
31
32
33
34
35
36
37
38
39
40
41
42
43
44
45
46
47
48
49
50
51
52
53
54
55
56
57
58
59
60

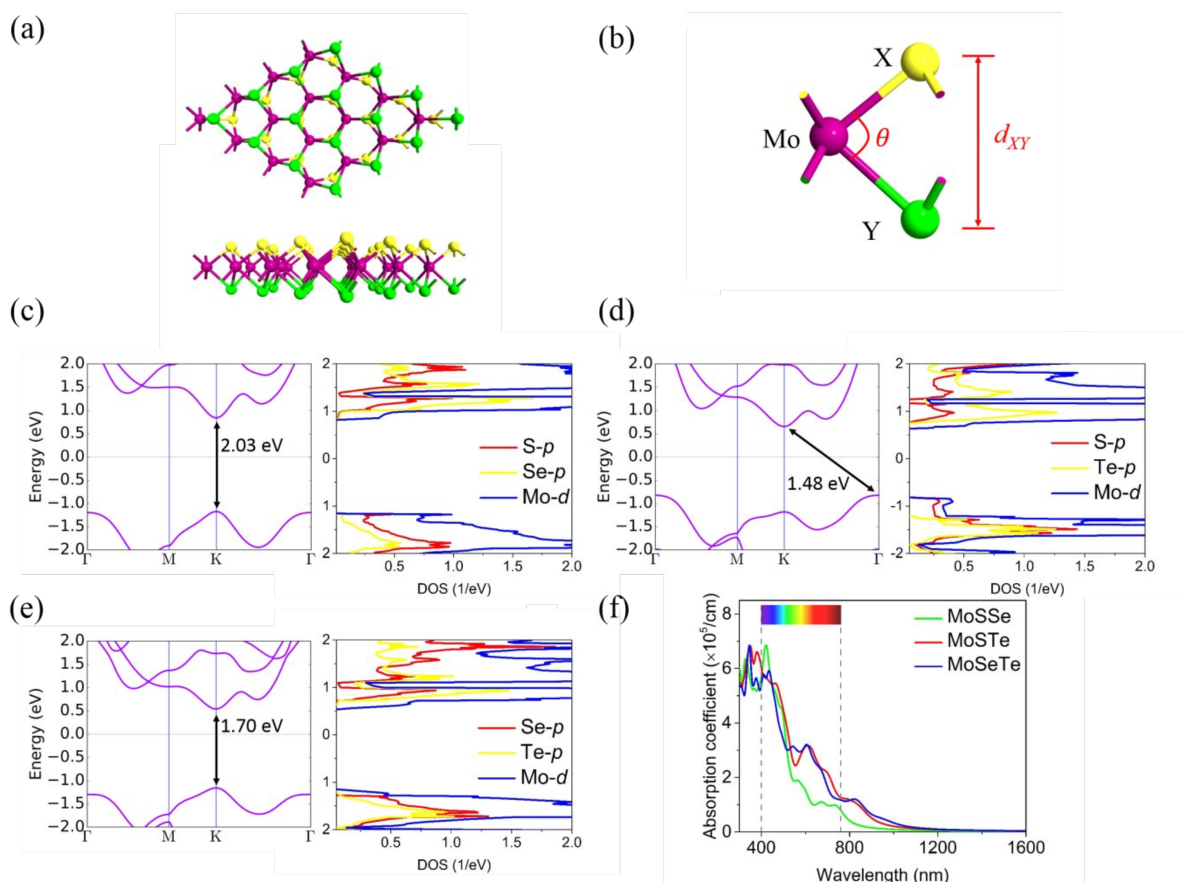

Figure 1. The geometry structure (a), distance between X and Y atom (b) of monolayer MoXY. (c), (d) and (e) are the band structure and projected density of state of monolayer MoSSe, MoSTe and MoSeTe. (f) is the optical absorption coefficient of monolayer MoXY.

Table 1. Lattice parameters (a). distance between X and Y atom (d_{X-Y}), bond angle (θ), bandgap (E_g), electrostatic potential difference ($\Delta\phi$), ionization potential (E_I) and electron affinity (E_A) for monolayer MoXY.

	a (Å)	d_{X-Y} (Å)	θ	E_g (eV)	$\Delta\phi$ (eV)	E_I (eV)	E_A (eV)
MoSSe	3.25	3.23	81.4°	2.03	0.77	5.66	3.71
MoSTe	3.36	3.37	81.6°	1.48	1.63	5.33	3.74
MoSeTe	3.43	3.48	82.4°	1.70	0.97	5.09	3.50

3.2 Crystal structure and electronic properties of graphene/MoXY heterostructures

As shown in Figure 2(a), we construct graphene/MoXY heterostructures by attaching monolayer graphene and monolayer MoXY together. The lattice match between the monolayer graphene and monolayer MoXY starts with the Generalized Lattice Match (GLM) method, which is for investigating the relationship between the mismatch strain and the number of atoms [57]. Because the size of graphene and monolayer MoXY surface cells are not commensurate, strain is needed to build up at the interface to tune the lattice constant for one surface, thereby obtaining a stable interface geometry. The aim of match angle optimization is targeted to have a lower mismatch strain and at the same time a smaller number of atoms.

1
2
3
4
5
6
7
8
9
10
11
12
13
14
15
16
17
18
19
20
21
22
23
24
25
26
27
28
29
30
31
32
33
34
35
36
37
38
39
40
41
42
43
44
45
46
47
48
49
50
51
52
53
54
55
56
57
58
59
60

As shown in the Figure 2(b), the vectors $\mathbf{u}_1$ and $\mathbf{u}_2$ define the surface cell of the monolayer MoXY layer while the vectors $\mathbf{v}_1$ and $\mathbf{v}_2$ define the surface cell of the monolayer graphene layer. From the affine transformation matrix **A**, we can obtain the relationship between $[\mathbf{u}_1, \mathbf{u}_2]$ and $[\mathbf{v}_1, \mathbf{v}_2]$ as:

$$\mathbf{A}[\mathbf{u}_1, \mathbf{u}_2] = [\mathbf{v}_1, \mathbf{v}_2] \quad (2)$$

The rotation matrix **U** and 2D strain tensor matrix **P** have the forms as:

$$\mathbf{U} = \begin{bmatrix} \cos(\phi) & -\sin(\phi) \\ \sin(\phi) & \cos(\phi) \end{bmatrix} \quad (3)$$

$$\mathbf{P} = \boldsymbol{U}^{T}\mathbf{A} = \begin{bmatrix} \mathbf{1} + \boldsymbol{\epsilon}_{xx} & \boldsymbol{\epsilon}_{xy} \\ \boldsymbol{\epsilon}_{xy} & \mathbf{1} + \boldsymbol{\epsilon}_{yy} \end{bmatrix} \quad (4)$$

where, $\phi = |\phi_a - \phi_b|/2$ is the interlayer angle between monolayer MoXY and monolayer graphene, ϕ_a is the angle between vectors $\mathbf{u}_1$ and $\mathbf{u}_2$, ϕ_b denotes the angle between vectors $\mathbf{v}_1$ and $\mathbf{v}_2$. Strain tensor matrix P is defined by the 2D strain tensor (ϵ) [57]. We choose to apply strains only in the MoXY surface because we are interested in the detailed band structures of the graphene. Due to the monolayer MoXY has different atoms (X or Y) on each side, so we construct two stacking types with the monolayer graphene, named as G/XMoY and G/YMoX, respectively. The optimized interlayer angles, match strains, interlayer distance and atoms number with different stacking types as shown in Table 2. The strain value is applied differently among different models because the lattice parameters of monolayer MoSSe, MoSTe and MoSeTe are different, which require different strains to build a stable interface with graphene. In previous research the mismatch strains of heterostructures are usually less than 3% [58-59]. However, in our heterostructures, the maximum strain of the lattice mismatch is around 1.54% (graphene/MoSeTe heterostructure), which means an acceptable lattice mismatch between these two layers.

.

1
2
3
4
5
6
7
8
9
10
11
12
13
14
15
16
17
18
19
20
21
22
23
24
25
26
27
28
29
30
31
32
33
34
35
36
37
38
39
40
41
42
43
44
45
46
47
48
49
50
51
52
53
54
55
56
57
58
59
60

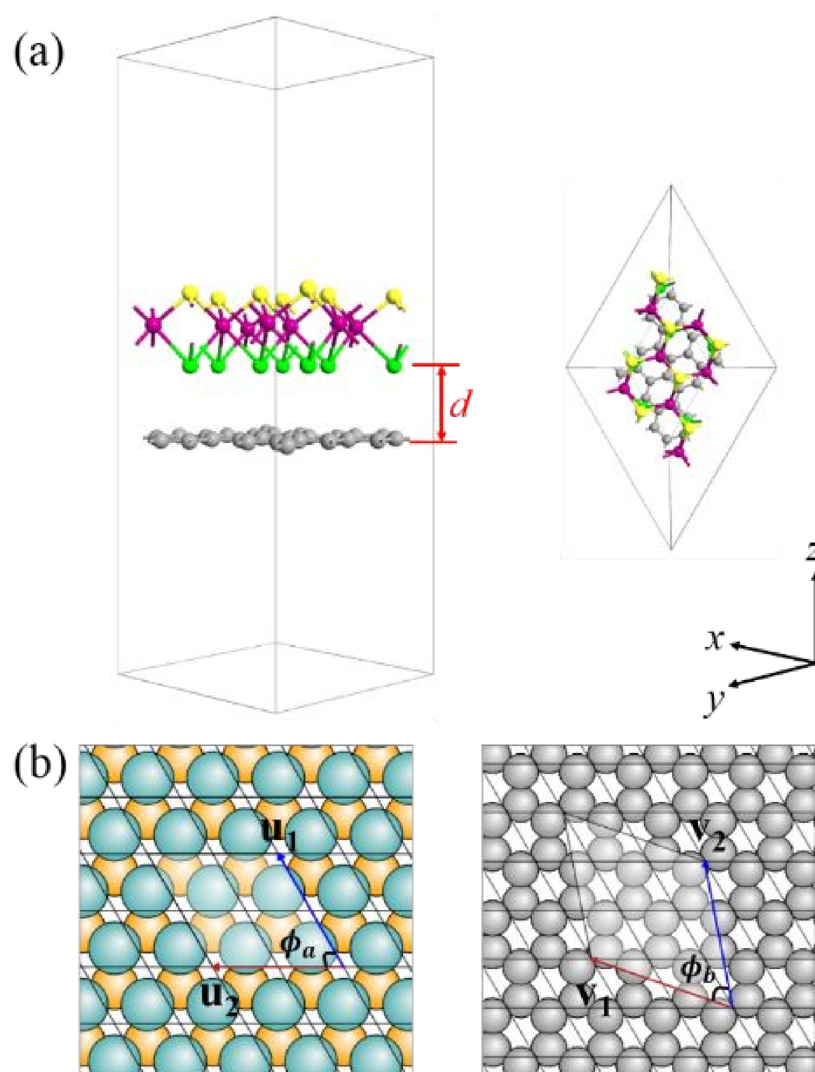

Figure 2. (a) shows the side and top view of the atomic arrangement of graphene/MoXY heterostructures, d indicates the distance between two layers. (b) shows the selected surface cell of MoXY and graphene.

Table 2. Interlayer angles, match strains, interlayer distance and atoms number of graphene/MoXY heterostructures.

	G/SMoSe	G/SeMoS	G/SMoTe	G/TeMoS	G/SeMoTe	G/TeMoSe
Interlayer angle	19.11^{o}	19.11^{o}	5.21^{o}	5.21^{o}	5.21^{o}	5.21^{o}
Match strain	0.10%	0.10%	0.18%	0.18%	1.54%	1.54%
Interlayer distance	3.27 Å	3.33 Å	3.50 Å	3.53 Å	3.51 Å	3.51 Å
Atoms number	26	26	47	47	47	47

1
2
3
4
5
6
7
8
9
10
11
12
13
14
15
16
17
18
19
20
21
22
23
24
25
26
27
28
29
30
31
32
33
34
35
36
37
38
39
40
41
42
43
44
45
46
47
48
49
50
51
52
53
54
55
56
57
58
59
60

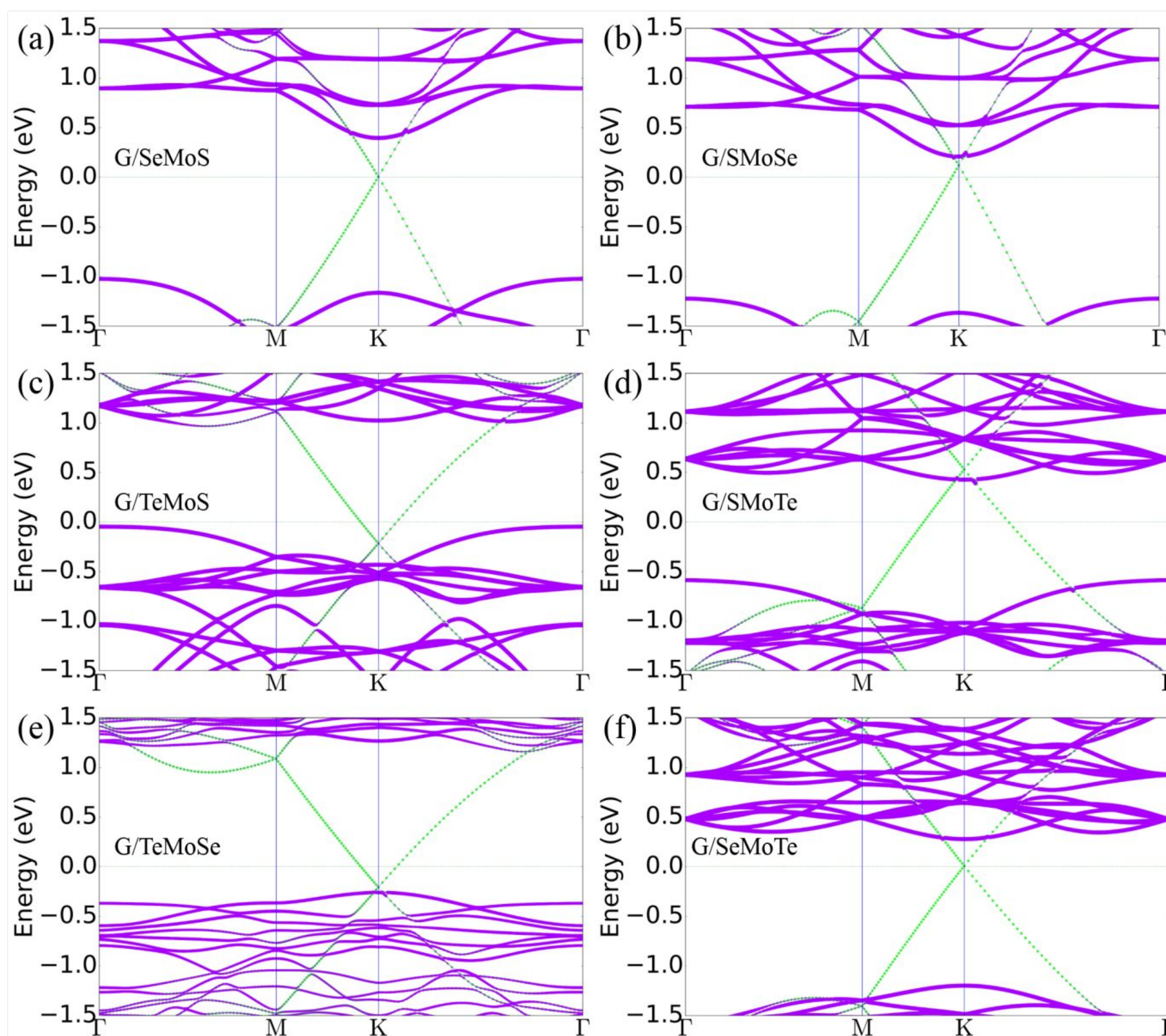

Figure 3. The computed fat band structure of G/SeMoS (a), G/SMoSe (b), G/TeMoS (c), G/SMoTe (d), G/TeMoSe(e) and G/SeMoTe (f). The green and purple lines represent the bands of graphene and MoXY.

Figure 3 shows the fat-band structure of graphene/MoXY heterostructures with six stacking types. The green and purple lines represent the bands of graphene and MoXY, respectively. Obviously, a Dirac cone is at the *K* point, which comes from the bands of graphene. Moreover, the VBM of MoSSe shifts from the *K* point (pristine monolayer MoSSe) to the *Γ* point, which is attributed to the band dispersion subject to the lattice strain of MoSSe layer. Although the CBM and the VBM of MoSTe and MoSeTe did not shift compared with the pristine monolayer cell, the position of bands changed under the lattice strain and the vdW interaction. Because the monolayer MoXY has an intrinsic dipole on the surface, inducing an internal electric field from Y atom to X atom. A small number of charges can cross the interlayer barrier between graphene layer and MoXY layer under the build-in electric field. Taking the G/TeMoS stacking as an example, under the 1.63 eV electrostatic potential difference ($\Delta\phi$) of monolayer MoSTe, electrons transfer from the valence band of monolayer MoSTe to the Dirac cone of graphene moving the tip of the Dirac cone under the Fermi level. The electrostatic potential difference of monolayer MoSSe and monolayer MoSeTe are 0.77

1
2
3
4
5
6
7
8
9
10
11
12
13
14
15
16
17
18
19
20
21
22
23
24
25
26
27
28
29
30
31
32
33
34
35
36
37
38
39
40
41
42
43
44
45
46
47
48
49
50
51
52
53
54
55
56
57
58
59
60

eV and 0.97 eV, respectively. We can see that the Graphene/MoSTe heterostructure has the largest Dirac cone shift in the Graphene/MoXY heterostructures. Comparing the band structures of the same Janus TMD layer with different stacking types (X or Y side to graphene), different band structures as shown in Figure 3(a) and (b) ((c) and (d), (e) and (f)) illustrate the necessity of building different stacking types.

In order to explore the potential nanoscale optical applications of graphene/MoXY heterostructures, we calculated the optical absorption coefficient with different stacking types. The optical properties of the heterostructures are mainly attributed to the band structures of MoXY. As shown in the Figure 4(a)-(c), graphene/MoXY heterostructures exhibit a broad absorption spectra range between ultraviolet light region and infrared light region. However, compared with the pristine monolayer MoXY, the optical absorption coefficient peak of the graphene/MoXY is lower. The physical mechanism is given as follows. The optical absorption coefficient of pristine monolayer MoXY and the graphene/MoXY heterostructure mainly come from the band extreme of these materials. Under the vdW interaction, the number of band extremes and the joint density of states decrease, which induced smaller probabilities of the electrons migrating across the bandgap. Interestingly, compared with the pristine monolayer MoSSe, the optical absorption coefficient is enhanced in the graphene/MoSSe heterostructure within the wavelength range from 550 nm to 800 nm (Figure 4(d)) and the absorption intensity can be higher than 10^5 /cm. Similarly results of the enhanced optical absorption coefficient by constructing a heterostructure can also be proposed in other 2D heterostructures [60-61]. Moreover, the optical absorption of G/SeMoS stacking type is higher than the G/SMoSe stacking type within the wavelength range from 550 nm to 800 nm. The high optical absorption coefficient and wide absorption wavelength in the visible light region will facilitate the graphene/MoSSe heterostructures being applied in the fields of optical sensors and photoelectrical detectors.

1
2
3
4
5
6
7
8
9
10
11
12
13
14
15
16
17
18
19
20
21
22
23
24
25
26
27
28
29
30
31
32
33
34
35
36
37
38
39
40
41
42
43
44
45
46
47
48
49
50
51
52
53
54
55
56
57
58
59
60

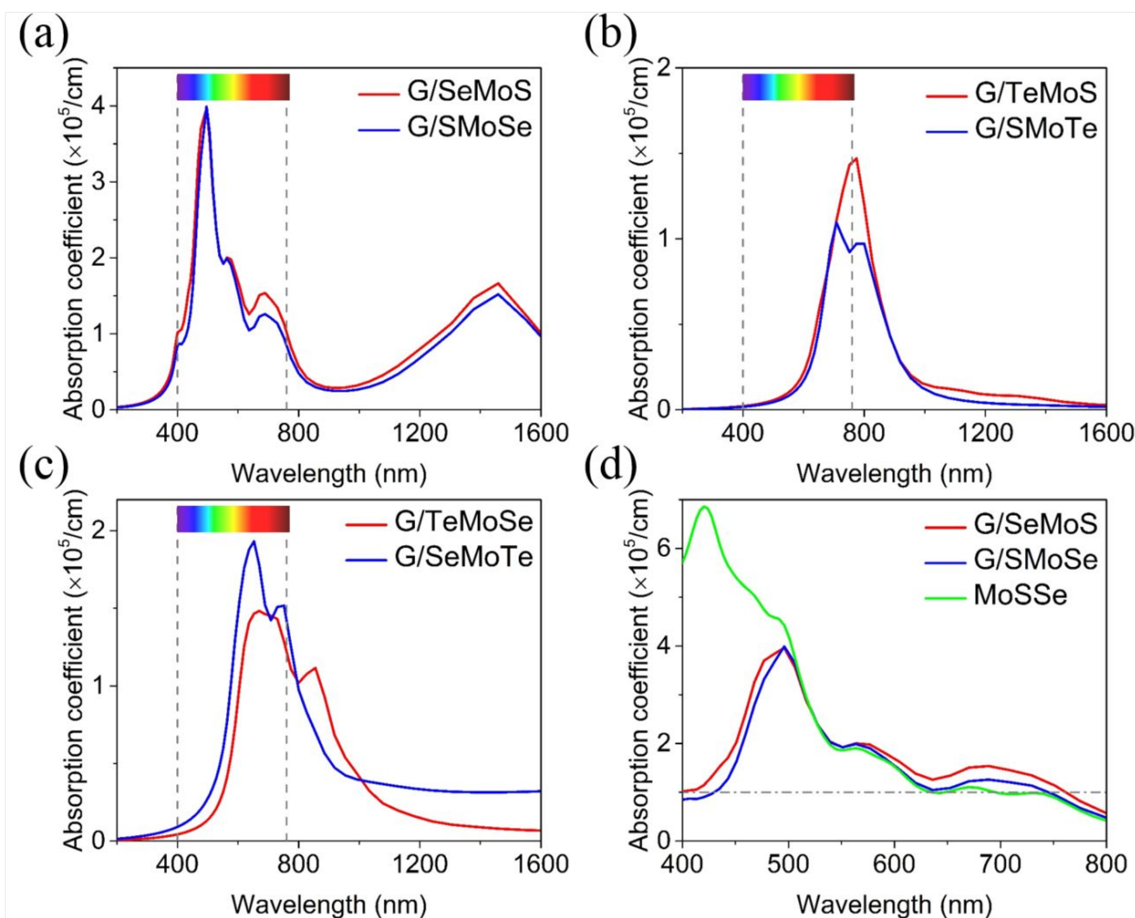

Figure 4. The optical absorption coefficient of graphene/MoSSe (a), graphene/MoSTe (b), graphene/MoSeTe (c), and pristine monolayer MoSSe (d).

To understand the physical origin of electronic and optical properties of graphene/MoXY heterostructures, we applied dipole correction in our DFT simulation. The charge density difference (Δn_e) of these heterostructures with different stacking types along *z*-direction in the Figure 5. The charge accumulation ($\Delta n_e > 0$) and depletion ($\Delta n_e < 0$) induce the charge redistribution process. Because of the surface charge repulsion effect between graphene layer and MoXY layer, a clear interlayer charge depletion appears between the *C* atom and *X(Y)* atom. Obviously, the graphene layer gains electrons and the X atom layer of MoXY monolayer loses electrons (gains holes), inducing in electron-hole puddles at the graphene/MoXY interface. A further Bader analysis has been performed, and it can be seen that there are about 0.02e, 0.02e and 0.01e transferring in the Graphene/MoSSe, Graphene/MoSTe and Graphene/MoSeTe interface, respectively. These effects induce new optical absorption properties of graphene/MoXY heterostructures shown in Figure 4, which is different from the monolayer MoXY in Figure 1(f). Accordingly, the rebuilt electron distribution causes the electrons transferring between MoXY layer and graphene layer, resulting in the electron-hole puddles at the graphene/MoXY interface. The charge redistribution accelerates the electrons polarization and builds an interlayer electric field between the graphene layer and MoXY layer. In the end, the heterogenous systems will achieve balance under the diffusion force. In summary, there are two factors that together

1
2
3
4
5
6
7
8
9
10
11
12
13
14
15
16
17
18
19
20
21
22
23
24
25
26
27
28
29
30
31
32
33
34
35
36
37
38
39
40
41
42
43
44
45
46
47
48
49
50
51
52
53
54
55
56
57
58
59
60

influence the interlayer coupling of graphene/MoXY heterostructures. The first is the intrinsic dipole in MoXY layer and the second is the interlayer dipole caused by the charge redistribution. As a result, these effects will induce new electrical and optical properties for the graphene/MoXY heterostructures.

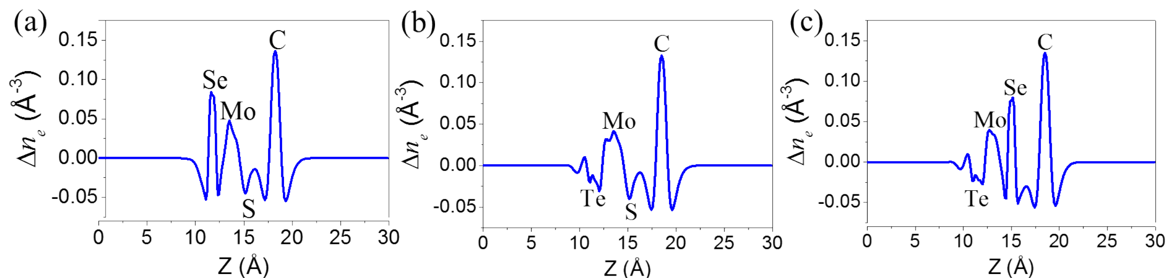

Figure 5. The computed charge density difference of Graphene/MoSSe (a), Graphene/MoSTe (b) and Graphene/MoSeTe (c) heterostructures along z-direction.

3.3 Modulate the doping of graphene by the interlayer distance and external electric field

The Dirac cone position of graphene in the vdW heterostructures is typically tunable under the external conditions, such as interlayer distance and external electric field [15, 32, 37, 41-42]. As shown in the Figure 6, electrons transfer from the valence band of monolayer MoXY to the Dirac cone of graphene moving the tip of the Dirac cone under the Fermi level, which is categorized as the electron doping (*e*-doping). Instead, the electrons transferred from the graphene to the monolayer MoXY move up the Dirac cone to above the Fermi level, named as the hole doping (*h*-doping). From the band structure of graphene/MoXY heterostructures under the different interlayer distance and external electric field, the shift of Dirac cone (E_D) relative to the Fermi level (E_F) can be calculated by $\Delta E_D = E_D - E_F$. From the linear dispersion around the Dirac cone of graphene, the charge carrier (electron or hole) density ($N_{h/e}$) of doped graphene can be calculated by [62]:

$$N_{h/e} = \frac{(\Delta E_D)^2}{\pi(\hbar v_F)^2} \quad (5)$$

where, $v_F = 1 \times 10^6 m/s$ is the Fermi velocity at the Dirac cone, $\hbar$ is the reduced Planck constant (1.055×10^{-34} J · s).

1
2
3
4
5
6
7
8
9
10
11
12
13
14
15
16
17
18
19
20
21
22
23
24
25
26
27
28
29
30
31
32
33
34
35
36
37
38
39
40
41
42
43
44
45
46
47
48
49
50
51
52
53
54
55
56
57
58
59
60

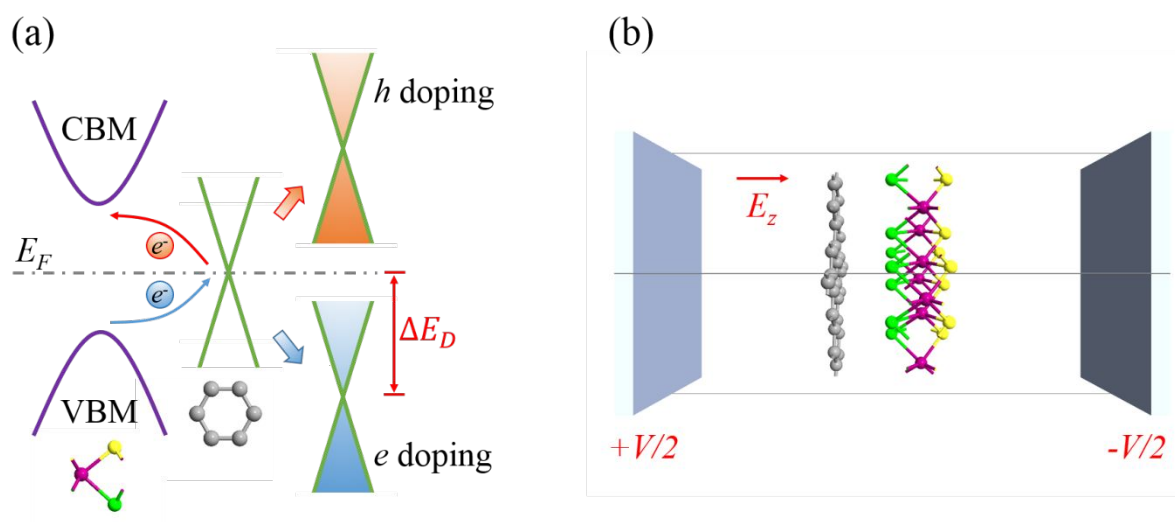

Figure 6. Doping of graphene (a) and external electric field (b) in the graphene/MoXY heterostructures.

In order to research the influence of interlayer distance (*d*) on the doping of graphene, the Dirac cone shift and carrier density as a function of the interlayer distance are shown in Figure 7. The interlayer distance varies from 2.5 Å to 4.5 Å. For the G/YMoX stacking type, the tip of the Dirac cone is above the Fermi level (hole doping) with the increase of interlayer distance. However, the tip of the Dirac cone is under the Fermi level (electron doping) with the increase of interlayer distance in the G/XMoY stacking type. In the Figure 7(a) and (b), the amplitude of Dirac cone shift in the G/SMoSe stacking type is higher than the G/SeMoS stacking at each considered interlayer distance, which means the carrier density of hole doping is always higher than the electron doping. When the interlayer distance increases from 2.5 Å, the carrier density of hole doping has immediately increased, while the carrier density of electron doping remains unchanged from 2.5 Å to 3.3 Å then slightly increases after 3.5 Å. The carrier density maximum of electron and hole doping are about $0.47 \times 10^{12}/cm^2$ and $1.89 \times 10^{12}/cm^2$ when the interlayer distance is about 4.0 Å. After that the carrier density decreases until the interlayer distance reaches 4.5 Å. For the graphene/MoSTe heterostructure, the change of Dirac cone position with interlayer distance is shown in Figure 7(c). Clearly, the biggest change is for the G/SMoTe stacking, which is about 0.18 eV, smaller than the 0.27 eV of G/TeMoS stacking type. Interestingly, Dirac cone is under the Fermi level for the interlayer distance between 2.5 Å and 4.5 Å for the G/TeMoS stacking, which means that the electron doping remains for each considered interlayer distance. In Figure 7(d), the highest carrier density of electron doping for G/TeMoS stacking type is about $5.39 \times 10^{12}/cm^2$ at 2.9 Å interlayer distance, which is 2.2 times higher than the carrier density of hole doping ($2.39 \times 10^{12}/cm^2$) with 3.5 Å and 3.7 Å interlayer distances for the G/SMoTe stacking. Moreover, the lowest carrier density of electron doping for the G/TeMoS stacking is $1.89 \times 10^{12}/cm^2$ at 4.1 Å interlayer distance and the carrier density is unaffected with the increase of interlayer distance until 4.5 Å. In Figure 7(e), the biggest Dirac cone shift for the G/SeMoTe stacking is about 0.04 eV at 4.1 Å and 4.3 Å, which is 3.8 times lower than the Dirac cone shift for the G/TeMoSe stacking (0.15 eV) at 2.9 Å and 3.1 Å interlayer distances. Just like the graphene/MoSTe, the position of Dirac cone in the G/TeMoSe stacking type is also under the Fermi level for each considered interlayer distance. Carrier density as a

1
2
3
4
5
6
7
8
9
10
11
12
13
14
15
16
17
18
19
20
21
22
23
24
25
26
27
28
29
30
31
32
33
34
35
36
37
38
39
40
41
42
43
44
45
46
47
48
49
50
51
52
53
54
55
56
57
58
59
60

function of interlayer distance for the graphene/MoSeTe is as shown in Figure 7(f). In the G/TeMoSe stacking, the carrier density of electron doping goes up quickly from 2.5 Å to 2.9 Å interlayer distance. After that, the carrier density stabilizes at around $1.67 \times 10^{12}/cm^2$. After 3.1 Å interlayer distance, the carrier density of electron doping decreases with the increase of interlayer distance and reaches to $0.07 \times 10^{12}/cm^2$ at 4.5 Å interlayer distance. For the G/SeMoTe stacking, although carrier density of hole doping changes with the increase of interlayer distance, the extent of change is far below the G/TeMoSe stacking. The peak carrier density of hole doping reaches to about $0.11 \times 10^{12}/cm^2$ at the 4.1 Å and 4.3 Å interlayer distance.

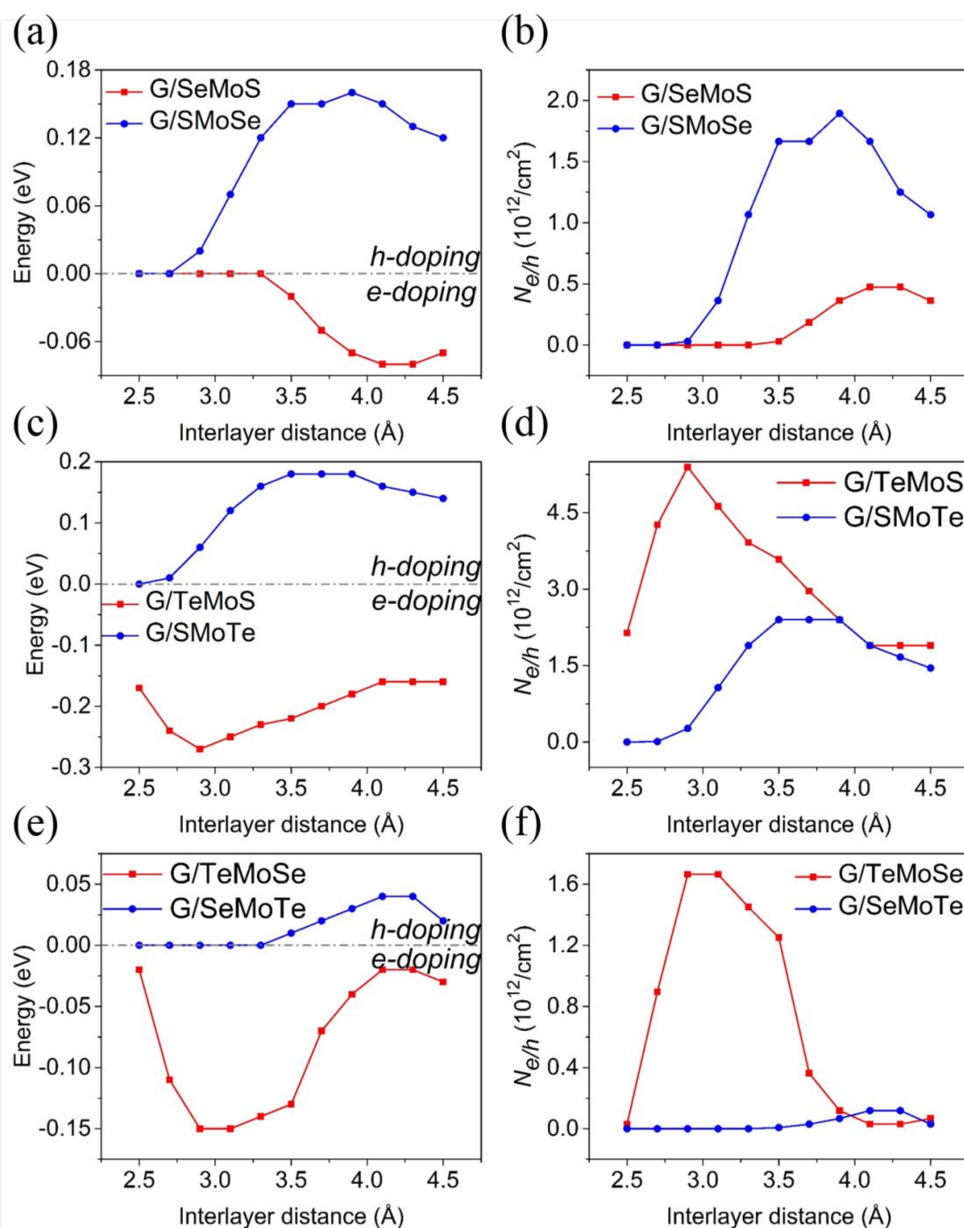

Figure 7. The Dirac cone shift and carrier density change in the graphene layer with interlayer distance increase for graphene/MoSSe (a, b), graphene/MoSTe (c, d) and graphene/MoSeTe (e, f) heterostructures.

1
2
3
4
5
6
7
8
9
10
11
12
13
14
15
16
17
18
19
20
21
22
23
24
25
26
27
28
29
30
31
32
33
34
35
36
37
38
39
40
41
42
43
44
45
46
47
48
49
50
51
52
53
54
55
56
57
58
59
60

Next, the effect of external electric field on the doping of graphene is investigated. An external electric field is applied as shown in Figure 6(b). The direction of the external electric field is defined as from the graphene layer to the MoXY layer. The unit of electric field is V/ Å rather than V because we define the electric field intensity rather than potential difference. Dirac cone shift and carrier density as a function of external electric field strength are as shown in Figure 8. In our research, the positive (negative) direction of external electric field is defined as from graphene (MoXY) layer to MoXY (graphene) layer and the strength of external electric field is in the range between -1.0 V/ Å and 1.0V/ Å. In Figure 8, the Dirac cone position of G/YMoX stacking is under the G/XMoY stacking at each considered electric field strength and all curves across the Fermi level, which means the Dirac cone can move up and down the Fermi level subject to the external electrical field. The heterostructure changes the graphene from hole doping to electron doping at electric field strength of -1.0 V/ Å to 1.0V/ Å. Moreover, a general trend as shown in the Figures 8(b), (d) and (f) that the carrier density increases with the rise of external electric field strength. In Figure 8(a), the maximum shift amplitudes of Dirac cone under the positive electric field are 0.60 eV and 0.31 eV for G/SeMoS and G/SMoSe stacking types, respectively. While under the -1 V/ Å electric field, the values are 0.38 eV (G/SeMoS) and 0.65 eV (G/SMoSe). Under the -0.2 V/ Å and 0 V/ Å, the Dirac cone of G/SeMoS stacking type remains on the Fermi level. However, for G/SMoSe stacking type, Dirac cone keeps on the Fermi level from 0.2 V/ Å to 0.4 V/ Å. For graphene/MoSSe heterostructures, the highest carrier density of electron doping for G/SeMoS and G/SMoSe stacking types are about $26.64 \times 10^{12}/cm^2$ and $7.11 \times 10^{12}/cm^2$, respectively (Figure 8(b)). In contrast, for the hole doping, the carrier density peaks are about $10.69 \times 10^{12}/cm^2$ and $31.27 \times 10^{12}/cm^2$ for G/SeMoS and the G/SMoSe stacking types, respectively. As shown in Figure 8(c), under the Fermi level, the biggest change of Dirac cone for G/TeMoS stacking type is about 0.79 eV, which is higher than the G/SMoTe stacking type. However, under the negative electric field, Dirac cone shifts to about 0.27 eV and 0.73 eV for G/TeMoS and G/SMoTe stacking types at the -1.0 V/ Å. From 0.2 V/ Å to 0.4 V/ Å, Dirac cone of G/SMoTe stacking type remains at the Fermi level. While for G/TeMoS stacking type, Dirac cone stays at the Fermi level under the -0.4 V/ Å. For positive electric field, the highest carrier density of electron doping for G/TeMoS and G/SMoTe stacking types are about $46.18 \times 10^{12}/cm^2$ and $20.01 \times 10^{12}/cm^2$, respectively. In contrast, under the negative electric field, the maximum carrier densities of hole doping are about $5.39 \times 10^{12}/cm^2$ (G/TeMoS) and $39.43 \times 10^{12}/cm^2$(G/SMoTe). For graphene/MoSeTe heterostructures, positive electric field causes the Dirac cone decline until -0.63 eV and -0.50 eV for G/TeMoSe and G/SeMoTe stacking types. However, the negative electric field induces the Dirac cone to increase to 0.30 eV and 0.65 eV for G/TeMoSe and G/SeMoTe stacking types. In Figure 8(f), the highest carrier densities of hole doping are about $6.66 \times 10^{12}/cm^2$ (G/TeMoSe) and $31.27 \times 10^{12}/cm^2$(G/SeMoTe) under the negative electric field, whereas the highest carrier densities of electron doping for G/TeMoSe and G/SeMoTe stacking types can achieve $29.37 \times 10^{12}/cm^2$ and $18.50 \times 10^{12}/cm^2$ under 1.0 V/ Å.

ACS Paragon Plus Environment

1
2
3
4
5
6
7
8
9
10
11
12
13
14
15
16
17
18
19
20
21
22
23
24
25
26
27
28
29
30
31
32
33
34
35
36
37
38
39
40
41
42
43
44
45
46
47
48
49
50
51
52
53
54
55
56
57
58
59
60

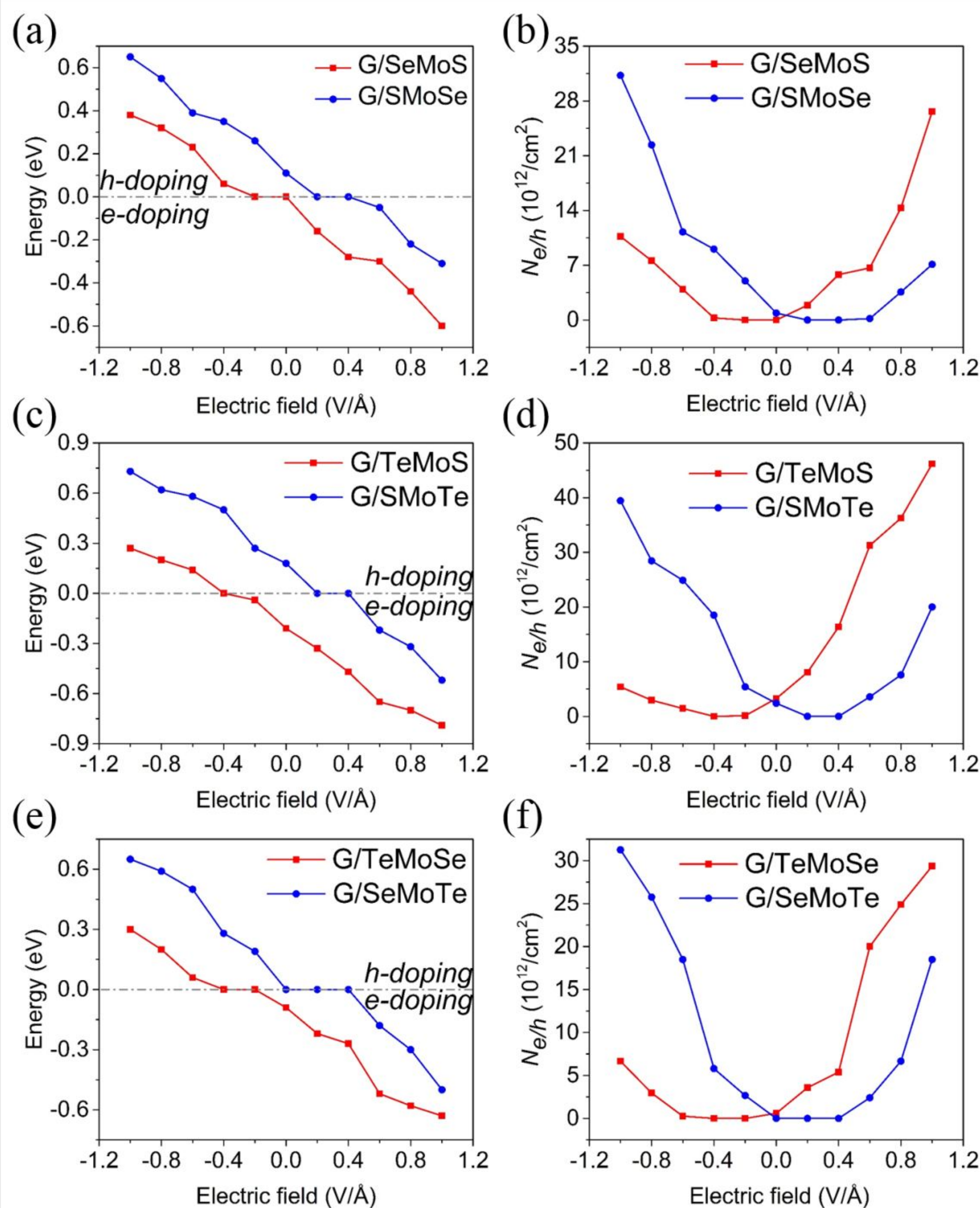

Figure 8. The shift of Dirac cone and carrier density change with the electric field strength for graphene/MoSSe (a, b), graphene/MoSTe (c, d) and graphene/MoSeTe (e, f) heterostructures.

Interlayer distance and external electric field are two effective ways to induced tunable doping in graphene for graphene/MoXY heterostructures. Compared with interlayer distance modulation, the influence of external electric field modulation is more pronounced. Because with a weak interaction of vdW, a small number of charges can cross the interlayer barrier between graphene layer and MoXY layer under the build-in electric field. However, under the external electric field, the electrostatic potential at the interlayer can enhance the charge transfer between bilayers. Taking the graphene/MoSSe as an example, the electrostatic potential (0.77 eV) and the electron affinity (3.71 eV) are shown in Table1. The electron affinity of the MoSSe monolayer is close to the work function of the graphene (4.30 eV) [15, 63], which means it is possible to transfer electrons between graphene layer and MoSSe layer. For

1
2
3
4
5
6
7
8
9
10
11
12
13
14
15
16
17
18
19
20
21
22
23
24
25
26
27
28
29
30
31
32
33
34
35
36
37
38
39
40
41
42
43
44
45
46
47
48
49
50
51
52
53
54
55
56
57
58
59
60

G/SMoSe stacking type, under the negative electric field, the electrons can be easily moved from Dirac cone to valence band because the external electric field has a same direction with the electrostatic potential of MoSSe (from Se atom to S atom). However, under the positive electric field, the electric field strength needs to be strong enough to offset the electrostatic potential of MoSSe and to make electrons overcome the bandgap of MoSSe (2.03 eV). As a result, the highest carrier density of G/SMoSe stacking type under the negative electric field ($37.27 \times 10^{12}/cm^2$) is higher than the positive electric field ($7.11 \times 10^{12}/cm^2$). In contrast, for the G/SeMoS stacking type, the highest carrier density under the negative electric field ($10.69 \times 10^{12}/cm^2$) is lower than the positive electric field ($26.64 \times 10^{12}/cm^2$). In the graphene/MoXY heterostructures, the highest carrier density of doping graphene is $4.62 \times 10^{13}/cm^2$ for G/TeMoS stacking type, which falls in between typical doping values of back gates or molecular doping ($\sim 10^{12}/cm^2$) [64-65] and ultrahigh doping obtained by electrolytic gating doping ($\sim 10^{14}/cm^2$) [66-67].

3.4 Interlayer distance, external electric field and strain effect the optical absorption of the graphene/MoSSe heterostructure

In the previous analysis, we find that the optical absorption coefficient of the graphene/MoSSe heterostructure is stronger than pristine monolayer MoSSe within the wavelength range from 550 nm to 800 nm (Figure 4(d)). Although the band structure of Graphene/MoXY heterostructures is a metal type, the Graphene/MoSSe heterostructures exhibit high optical absorption coefficients (greater than 10^5/cm in the wavelength range of 550 nm to 800 nm), which is attributed to the band structure of the MoSSe. Now, we investigate the interlayer distance influences on the optical absorption of graphene/MoSSe heterostructure. As shown in Figure 9(a) and (b), we simulated the optical absorption coefficient of the graphene/MoSSe with the G/SeMoS stacking type and G/SMoSe stacking type, respectively. Obviously, the simulation results show that a strong optical absorption coefficient (>1×10^5/cm) can be found in the visible light region for different interlayer distances. In Figure 9(a), we find that the absorption spectra for G/SeMoS stacking type is sensitive to the interlayer distance from 500 nm to 760 nm. However, for G/SMoSe stacking type, the optical absorption coefficient is insensitive to the interlayer distance between 500 nm and 760 nm. Interestingly, for the graphene/MoSSe heterostructure, the optical absorption coefficient has a trend of $\alpha_{a-2.9} > \alpha_{a-3.3} > \alpha_{a-3.7}$ in the visible region, which demonstrates a stronger interlayer coupling, which results in a higher optical absorption coefficient.

The influences of external electric field on the optical absorption properties of graphene/MoSSe heterostructure are also investigated under the -0.4 V/ Å, 0 V/ Å and 0.4 V/ Å. In the Figure 9(c), the results show that the optical absorption coefficient for G/SeMoS stacking type is sensitive to the external electric field strength within the wavelength range from 500 nm to 760 nm. While in Figure 9(d), for the G/SMoSe stacking type, the optical absorption coefficient is insensitive with the negative electric field in the visible region. Compared with -0.4 V/ Å and 0 V/ Å, the optical absorption coefficient under the 0.4 V/ Å

electric field is higher.

The strain-dependent optical absorption coefficient of graphene/MoSSe heterostructure is also analyzed as shown in Figures 9(e) and (f). The symmetric biaxial external deformations with -3% (compressive strain), 0 and 3% (tensile strain) are applied. The magnitude of strain is defined as $\Delta\varepsilon = (a - a_0)/a_0$, where a_0 and a are the equilibrium and strained lattice values, respectively. In the Figures 9(e) and (f), the observation reveals that the absorption spectrum shifts toward longer wavelengths (red-shift) under the strains, which is consistent with the prior researches [23, 68]. Compared with the compressive strain, the shift of optical absorption spectra under the tensile strain is more significant. These new properties indicate that the Graphene/MoSSe heterostructure will have potential applications in nanoscale optical sensors.

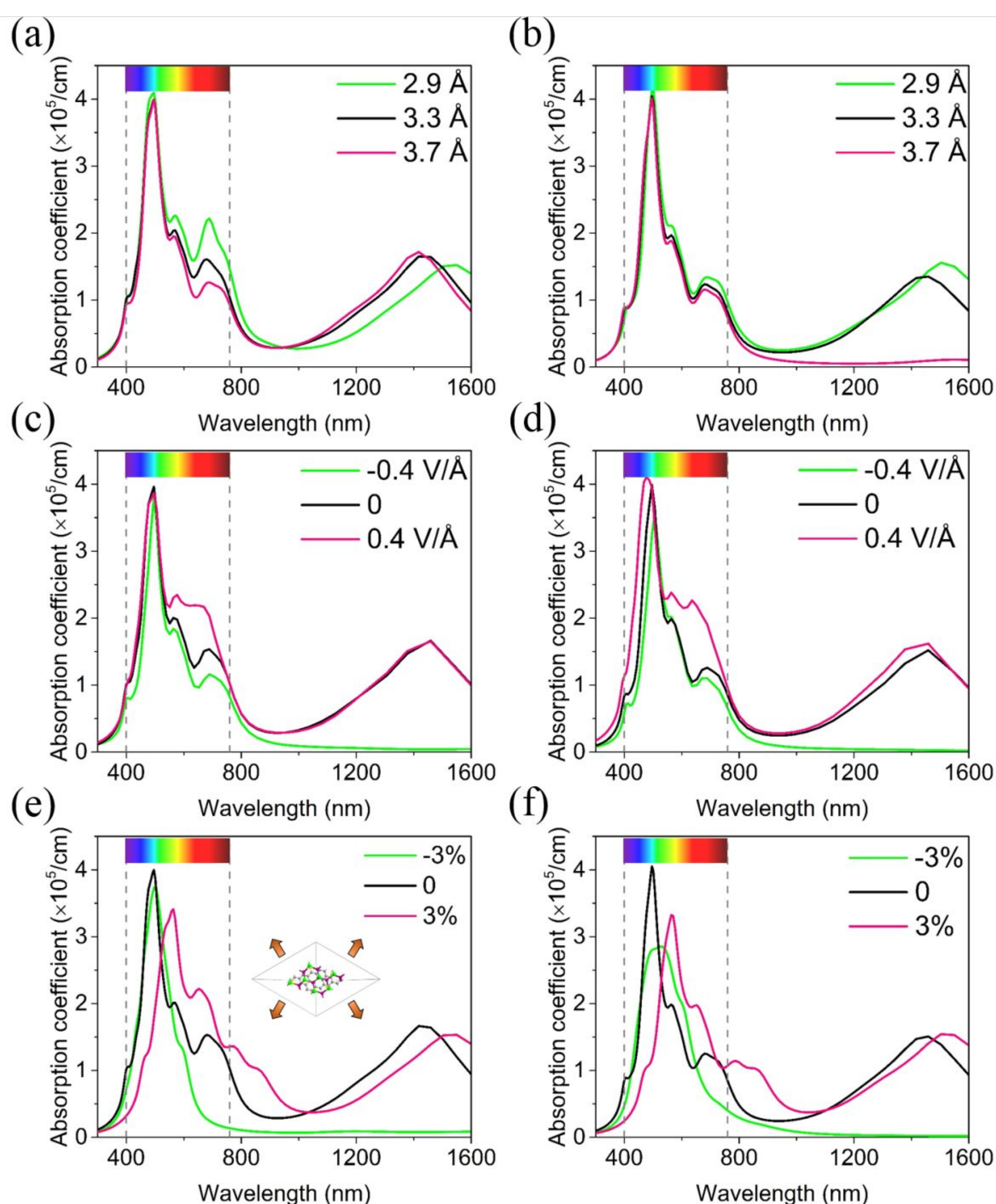

Figure 9. The interlayer distance (a, b), external electric field (c, d) and strain effect (e, f) on the optical absorption coefficient for G/SeMoS (a, c, e) and G/SMoSe (b, d, f) stacking types.

1
2
3
4
5
6
7
8
9
10
11
12
13
14
15
16
17
18
19
20
21
22
23
24
25
26
27
28
29
30
31
32
33
34
35
36
37
38
39
40
41
42
43
44
45
46
47
48
49
50
51
52
53
54
55
56
57
58
59
60

4. CONCLUSION

In this work, the electronic and optical properties of graphene/MoXY heterostructures under interlayer distance, external electric field and strain effect are analyzed by the first principle methods. Results show that interlayer distance and external electric field are two effective ways to induce tunable doping in the graphene layer. Compared with the interlayer distance modulation, influence of external electric field modulation is much more pronounced. In the graphene/MoXY heterostructures, the highest carrier density of graphene can be achieved to be $4.62 \times 10^{13}/cm^2$ for the G/TeMoS stacking type under the 1.0V/ Å electric field strength. In addition, compared with the pristine monolayer MoSSe, the optical absorption coefficient is enhanced by the graphene/MoSSe heterostructure within the wavelength range from 550 nm to 800 nm and the absorption coefficient is higher than 10^5 /cm. Moreover, the optical absorption spectra of the graphene/MoSSe heterostructures can be easily modulated by interlayer distance, external electric field and mechanical strain. These results imply that potential applications in tunable nanoelectronic and photovoltaic devices can be explored with these techniques.

CONFLICT OF INTEREST

There are no conflicts to declare.

ACKNOWLEDGEMENTS

Authors are grateful for funding by the China Scholarship Council (CSC). The authors would like to acknowledge the European Regional Development Fund (ERDF) for the funding of the Solar Photovoltaic Academic Research Consortium (SPARC II) which supported this research.

REFERENCES

(1) Novoselov, K. S.; Geim, A. K.; Morozov, S. V.; Jiang, D.; Zhang, Y.; Dubonos, S. V.; Grigorieva, I. V.; Firsov, A. A. Electric Field Effect in Atomically Thin Carbon Films. *Science* **2004**, *306,* 666-669.

(2) Bolotin, K. I.; Sikes, K. J.; Jiang, Z.; Klima, M.; Fudenberg, G.; Hone, J.; Kim, P.; Stormer, H. L. Ultrahigh Electron Mobility in Suspended Graphene. *Solid State Commun.* **2008**, *146,* 351-355.

(3) Banszerus, L.; Schmitz, M.; Engels, S.; Dauber, J.; Oellers, M.; Haupt, F.; Watanabe, K.; Taniguchi, T.; Beschoten, B.; Stampfer, C. Ultrahigh-Mobility Graphene Devices from Chemical Vapor Deposition on Reusable Copper. *Sci. Adv.* **2015**, *1,* 1-6.

(4) Banszerus, L.; Schmitz, M.; Engels, S.; Goldsche, M.; Watanabe, K.; Taniguch, T.; Beschoten, B.; Stampfer, C. Ballistic Transport Exceeding 28 μm in CVD Grown Graphene. *Nano Lett.* **2016**, *16,* 1387-1391.

(5) Zuev, Y. M.; Chang, W.; Kim, P. Thermoelectric and Magnetothermoelectric Transport Measurements of Graphene. *Phys. Rev. Lett.* **2009**, *102,* 096807.

(6) Castro Neto, A. H.; Guinea, F.; Peres, N. M. R.; Novoselov, K. S.; Geim, A. K. The Electronic Properties of Graphene. *Rev. Mod. Phys.* **2009**, *81,* 109-162.

(7) Balandin, A. A.; Ghosh, S.; Bao, W. Z.; Calizo, I.; Teweldebrhan, D.; Miao, F.; Lau, C. N.

1
2
3
4
5
6
7
8
9
10
11
12
13
14
15
16
17
18
19
20
21
22
23
24
25
26
27
28
29
30
31
32
33
34
35
36
37
38
39
40
41
42
43
44
45
46
47
48
49
50
51
52
53
54
55
56
57
58
59
60

Superior Thermal Conductivity of Single-Layer Graphene. *Nano Lett.* **2008**, *8,* 902-907.
(8) Kim, K. S.; Zhao, Y.; Jang, H.; Lee, S. Y.; Kim, J. M.; Kim, K. S.; Ahn, J. H.; Kim, P.; Choi, J. Y.; Hong, B. H. Large-Scale Pattern Growth of Graphene Films for Stretchable Transparent Electrodes. *Nature* **2009**, *457,* 706-710.
(9) Jang, H.; Park, Y. J.; Chen, X.; Das, T.; Kim, M. S.; Ahn, J. H. Graphene-Based Flexible and Stretchable Electronics. *Adv. Mater.* **2016**, *28,* 4184-4202.
(10) Jang, M. S.; Kim, H.; Son, Y.-W.; Atwater, H. A.; Goddard, W. A. Graphene Field Effect Transistor without an Energy Gap. *Proceedings of the National Academy of Sciences* **2013**, *110,* 8786-8789.
(11) Watanabe, K.; Taniguchi, T.; Kanda, H. Direct-Bandgap Properties and Evidence for Ultraviolet Lasing of Hexagonal Boron Nitride Single Crystal. *Nat. Mater.* **2004**, *3,* 404-409.
(12) Shi, Y. M.; Hamsen, C.; Jia, X. T.; Kim, K. K.; Reina, A.; Hofmann, M.; Hsu, A. L.; Zhang, K.; Li, H. N.; Juang, Z. Y.; Dresselhaus, M. S.; Li, L. J.; Kong, J. Synthesis of Few-Layer Hexagonal Boron Nitride Thin Film by Chemical Vapor Deposition. *Nano Lett.* **2010**, *10,* 4134-4139.
(13) Mak, K. F.; Lee, C.; Hone, J.; Shan, J.; Heinz, T. F. Atomically Thin MoS2: A New Direct-Gap Semiconductor. *Phys. Rev. Lett.* **2010**, *105,* 136805.
(14) Radisavljevic, B.; Radenovic, A.; Brivio, J.; Giacometti, V.; Kis, A. Single-Layer MoS2 Transistors. *Nature Nanotechnology* **2011**, *6,* 147-150.
(15) Choi, M. S.; Lee, G. H.; Yu, Y. J.; Lee, D. Y.; Lee, S. H.; Kim, P.; Hone, J.; Yoo, W. J. Controlled Charge Trapping by Molybdenum Disulphide and Graphene in Ultrathin Heterostructured Memory Devices. *Nat. Commun.* **2013**, *4,* 1-7.
(16) Li, L. K.; Yu, Y. J.; Ye, G. J.; Ge, Q. Q.; Ou, X. D.; Wu, H.; Feng, D. L.; Chen, X. H.; Zhang, Y. B. Black Phosphorus Field-Effect Transistors. *Nat. Nanotechnol.* **2014**, *9,* 372-377.
(17) Qiao, J. S.; Kong, X. H.; Hu, Z. X.; Yang, F.; Ji, W. High-Mobility Transport Anisotropy and Linear Dichroism in Few-Layer Black Phosphorus. *Nat. Commun.* **2014**, *5,* 1-7.
(18) Lu, A. Y.; Zhu, H. Y.; Xiao, J.; Chuu, C. P.; Han, Y. M.; Chiu, M. H.; Cheng, C. C.; Yang, C. W.; Wei, K. H.; Yang, Y. M.; Wang, Y.; Sokaras, D.; Nordlund, D.; Yang, P. D.; Muller, D. A.; Chou, M. Y.; Zhang, X.; Li, L. J. Janus Monolayers of Transition Metal Dichalcogenides. *Nat. Nanotechnol.* **2017**, *12,* 744-+.
(19) Cheng, Y. C.; Zhu, Z. Y.; Tahir, M.; Schwingenschlogl, U. Spin-Orbit-Induced Spin Splittings in Polar Transition Metal Dichalcogenide Monolayers. *Epl-Europhys Lett* **2013**, *102,* 57001.
(20) Zhang, J.; Jia, S.; Kholmanov, I.; Dong, L.; Er, D. Q.; Chen, W. B.; Guo, H.; Jin, Z. H.; Shenoy, V. B.; Shi, L.; Lou, J. Janus Monolayer Transition-Metal Dichalcogenides. *ACS Nano* **2017**, *11,* 8192-8198.
(21) Dong, L.; Lou, J.; Shenoy, V. B. Large in-Plane and Vertical Piezoelectricity in Janus Transition Metal Dichalchogenides. *ACS Nano* **2017**, *11,* 8242-8248.
(22) Ji, Y. J.; Yang, M. Y.; Lin, H. P.; Hou, T. J.; Wang, L.; Li, Y. Y.; Lee, S. T. Janus Structures of Transition Metal Dichalcogenides as the Heterojunction Photocatalysts for Water Splitting. *J. Phys. Chem. C* **2018**, *122,* 3123-3129.
(23) Ma, X. C.; Wu, X.; Wang, H. D.; Wang, Y. C. A Janus Mosse Monolayer: A Potential Wide Solar-Spectrum Water-Splitting Photocatalyst with a Low Carrier Recombination Rate. *J Mater Chem A* **2018**, *6,* 2295-2301.
(24) Guan, Z. Y.; Ni, S.; Hu, S. L. Tunable Electronic and Optical Properties of Monolayer and

Multilayer Janus Mosse as a Photocatalyst for Solar Water Splitting: A First-Principles Study. *J. Phys. Chem. C* **2018**, *122,* 6209-6216.
(25) Wen, Y. N.; Xia, M. G.; Zhang, S. L. Bandgap Engineering of Janus Mosse Monolayer Implemented by Se Vacancy. *Comp Mater Sci* **2018**, *152,* 20-27.
(26) Li, F. P.; Wei, W.; Zhao, P.; Huang, B. B.; Dai, Y. Electronic and Optical Properties of Pristine and Vertical and Lateral Heterostructures of Janus Mosse and Wsse. *J. Phys. Chem. Lett.* **2017**, *8,* 5959-5965.
(27) Liang, Y.; Li, J. W.; Jin, H.; Huang, B. B.; Dai, Y. Photoexcitation Dynamics in Janus-MoSSe/WSe2 Heterobilayers: Ab Initio Time-Domain Study. *J. Phys. Chem. Lett.* **2018**, *9,* 2797-2802.
(28) Palsgaard, M.; Gunst, T.; Markussen, T.; Thygesen, K. S.; Brandbyge, M. Stacked Janus Device Concepts: Abrupt PN-Junctions and Cross-Plane Channels. *Nano Lett.* **2018**, *18,* 7275-7281.
(29) Dean, C. R.; Young, A. F.; Meric, I.; Lee, C.; Wang, L.; Sorgenfrei, S.; Watanabe, K.; Taniguchi, T.; Kim, P.; Shepard, K. L.; Hone, J. Boron Nitride Substrates for High-Quality Graphene Electronics. *Nat. Nanotechnol.* **2010**, *5,* 722-726.
(30) Xue, J. M.; Sanchez-Yamagishi, J.; Bulmash, D.; Jacquod, P.; Deshpande, A.; Watanabe, K.; Taniguchi, T.; Jarillo-Herrero, P.; Leroy, B. J. Scanning Tunnelling Microscopy and Spectroscopy of Ultra-Flat Graphene on Hexagonal Boron Nitride. *Nat. Mater.* **2011**, *10,* 282-285.
(31) Giovannetti, G.; Khomyakov, P. A.; Brocks, G.; Kelly, P. J.; van den Brink, J. Substrate-Induced Band Gap in Graphene on Hexagonal Boron Nitride: Ab Initio Density Functional Calculations. *Phys. Rev. B* **2007**, *76,* 073103.
(32) Sachs, B.; Britnell, L.; Wehling, T. O.; Eckmann, A.; Jalil, R.; Belle, B. D.; Lichtenstein, A. I.; Katsnelson, M. I.; Novoselov, K. S. Doping Mechanisms in Graphene-MoS2 Hybrids. *Appl. Phys. Lett.* **2013**, *103,* 251607.
(33) Britnell, L.; Gorbachev, R. V.; Jalil, R.; Belle, B. D.; Schedin, F.; Mishchenko, A.; Georgiou, T.; Katsnelson, M. I.; Eaves, L.; Morozov, S. V.; Peres, N. M. R.; Leist, J.; Geim, A. K.; Novoselov, K. S.; Ponomarenko, L. A. Field-Effect Tunneling Transistor Based on Vertical Graphene Heterostructures. *Science* **2012**, *335,* 947-950.
(34) Roy, K.; Padmanabhan, M.; Goswami, S.; Sai, T. P.; Ramalingam, G.; Raghavan, S.; Ghosh, A. Graphene-MoS2 Hybrid Structures for Multifunctional Photoresponsive Memory Devices. *Nat. Nanotechnol.* **2013**, *8,* 826-830.
(35) Britnell, L.; Ribeiro, R. M.; Eckmann, A.; Jalil, R.; Belle, B. D.; Mishchenko, A.; Kim, Y. J.; Gorbachev, R. V.; Georgiou, T.; Morozov, S. V.; Grigorenko, A. N.; Geim, A. K.; Casiraghi, C.; Castro Neto, A. H.; Novoselov, K. S. Strong Light-Matter Interactions in Heterostructures of Atomically Thin Films. *Science* **2013**, *340,* 1311-1314.
(36) Yu, W. J.; Li, Z.; Zhou, H. L.; Chen, Y.; Wang, Y.; Huang, Y.; Duan, X. F. Vertically Stacked Multi-Heterostructures of Layered Materials for Logic Transistors and Complementary Inverters. *Nat. Mater.* **2013**, *12,* 246-252.
(37) Hu, W.; Wang, T.; Zhang, R. Q.; Yang, J. L. Effects of Interlayer Coupling and Electric Fields on the Electronic Structures of Graphene and MoS2 Heterobilayers. *J. Mater. Chem. C* **2016**, *4,* 1776-1781.
(38) Avsar, A.; Vera-Marun, I. J.; Tan, J. Y.; Watanabe, K.; Taniguchi, T.; Neto, A. H. C.;

ACS Paragon Plus Environment

1
2
3
4
5
6
7
8
9
10
11
12
13
14
15
16
17
18
19
20
21
22
23
24
25
26
27
28
29
30
31
32
33
34
35
36
37
38
39
40
41
42
43
44
45
46
47
48
49
50
51
52
53
54
55
56
57
58
59
60

Ozyilmaz, B. Air-Stable Transport in Graphene-Contacted, Fully Encapsulated Ultrathin Black Phosphorus-Based Field-Effect Transistors. *ACS Nano* **2015**, *9,* 4138-4145.
(39) Padilha, J. E.; Fazzio, A.; da Silva, A. J. R. Van Der Waals Heterostructure of Phosphorene and Graphene: Tuning the Schottky Barrier and Doping by Electrostatic Gating. *Phys. Rev. Lett.* **2015**, *114,* 066803.
(40) Kim, W.; Li, C. F.; Chaves, F. A.; Jimenez, D.; Rodriguez, R. D.; Susoma, J.; Fenner, M. A.; Lipsanen, H.; Riikonen, J. Tunable Graphene-Gase Dual Heterojunction Device. *Adv. Mater.* **2016**, *28,* 1845-1852.
(41) Pham, K. D.; Hieu, N. N.; Phuc, H. V.; Hoi, B. D.; Ilysov, V. V.; Amin, B.; Nguyen, C. V. First Principles Study of the Electronic Properties and Schottky Barrier in Vertically Stacked Graphene on the Janus Moses under Electric Field. *Comp Mater Sci* **2018**, *153,* 438-444.
(42) Li, Y.; Wang, J. J.; Zhou, B. Z.; Wang, F.; Miao, Y. P.; Wei, J. Q.; Zhang, B. J.; Zhang, K. L. Tunable Interlayer Coupling and Schottky Barrier in Graphene and Janus MoSSe Heterostructures by Applying an External Field. *Phys. Chem. Chem. Phys.* **2018**, *20,* 24109-24116.
(43) Pham, K. D.; Hieu, N. N.; Phuc, H. V.; Fedorov, I. A.; Duque, C. A.; Amin, B.; Nguyen, C. V. Layered Graphene/GaS Van Der Waals Heterostructure: Controlling the Electronic Properties and Schottky Barrier by Vertical Strain. *Appl. Phys. Lett.* **2018**, *113,* 171605.
(44) Le, P. T. T.; Hieu, N. N.; Bui, L. M.; Phuc, H. V.; Hoi, B. D.; Amin, B.; Nguyen, C. V. Structural and Electronic Properties of a Van Der Waals Heterostructure Based on Silicene and Gallium Selenide: Effect of Strain and Electric Field. *Phys. Chem. Chem. Phys.* **2018**, *20,* 27856-27864.
(45) Deng, S.; Zhang, Y.; Li, L. J. Study on Electronic and Optical Properties of the Twisted and Strained MoS2/PtS2 Heterogeneous Interface. *Appl. Surf. Sci.* **2019**, *476,* 308-316.
(46) He, Y. M.; Yang, Y.; Zhang, Z. H.; Gong, Y. J.; Zhou, W.; Hu, Z. L.; Ye, G. L.; Zhaug, X.; Bianco, E.; Lei, S. D.; Jin, Z. H.; Zou, X. L.; Yang, Y. C.; Zhang, Y.; Xie, E. Q.; Lou, J.; Yakobson, B.; Vajtai, R.; Li, B.; Ajayan, P. Strain-Induced Electronic Structure Changes in Stacked Van Der Waals Heterostructures. *Nano Lett.* **2016**, *16,* 3314-3320.
(47) Rathi, S.; Lee, I.; Lim, D.; Wang, J. W.; Ochiai, Y.; Aoki, N.; Watanabe, K.; Taniguchi, T.; Lee, G. H.; Yu, Y. J.; Kim, P.; Kim, G. H. Tunable Electrical and Optical Characteristics in Mono Layer Graphene and Few-Layer Mos2 Heterostructure Devices. *Nano Lett.* **2015**, *15,* 5017-5024.
(48) Tongay, S.; Fan, W.; Kang, J.; Park, J.; Koldemir, U.; Suh, J.; Narang, D. S.; Liu, K.; Ji, J.; Li, J. B.; Sinclair, R.; Wu, J. Q. Tuning Interlayer Coupling in Large-Area Heterostructures with CVD-Grown MoS2 and WS2 Monolayers. *Nano Lett.* **2014**, *14,* 3185-3190.
(49) *Atomistix ToolKit (ATK),* https://quantumwise.com/. .
(50) Grimme, S. Semiempirical GGA-Type Density Functional Constructed with a Long-Range Dispersion Correction. *J Comput Chem* **2006**, *27,* 1787-1799.
(51) Zhang, L. S.; Dai, X. Y.; Li, T.; Li, H. Chemical Modification, Field Effect Transistor and Voltage-Driven Spin Logic Gates of Tailored Monolayer Mos2 Nanoflakes. *Appl. Surf. Sci.* **2019**, *481,* 910-918.
(52) Haastrup, S.; Strange, M.; Pandey, M.; Deilmann, T.; Schmidt, P. S.; Hinsche, N. F.; Gjerding, M. N.; Torelli, D.; Larsen, P. M.; Riis-Jensen, A. C.; Gath, J.; Jacobsen, K. W.; Mortensen, J. J.; Olsen, T.; Thygesen, K. S. The Computational 2d Materials Database:

1
2
3
4
5
6
7
8
9
10
11
12
13
14
15
16
17
18
19
20
21
22
23
24
25
26
27
28
29
30
31
32
33
34
35
36
37
38
39
40
41
42
43
44
45
46
47
48
49
50
51
52
53
54
55
56
57
58
59
60

High-Throughput Modeling and Discovery of Atomically Thin Crystals. *2D Materials* **2018**, *5,* 042002.
(53) Luftner, D.; Refaely-Abramson, S.; Pachler, M.; Resel, R.; Ramsey, M. G.; Kronik, L.; Puschnig, P. Experimental and Theoretical Electronic Structure of Quinacridone. *Phys. Rev. B* **2014**, *90,* 075204.
(54) Huang, X.; Paudel, T. R.; Dong, S.; Tsymbal, E. Y. Hexagonal Rare-Earth Manganites as Promising Photovoltaics and Light Polarizers. *Phys. Rev. B* **2015**, *92,* 125201.
(55) Er, D. Q.; Ye, H.; Frey, N. C.; Kumar, H.; Lou, J.; Shenoy, V. B. Prediction of Enhanced Catalytic Activity for Hydrogen Evolution Reaction in Janus Transition Metal Dichalcogenides. *Nano Lett.* **2018**, *18,* 3943-3949.
(56) Wang, J.; Shu, H. B.; Zhao, T. F.; Liang, P.; Wang, N.; Cao, D.; Chen, X. S. Intriguing Electronic and Optical Properties of Two-Dimensional Janus Transition Metal Dichalcogenides. *Phys. Chem. Chem. Phys.* **2018**, *20,* 18571-18578.
(57) Jelver, L.; Larsen, P. M.; Stradi, D.; Stokbro, K.; Jacobsen, K. W. Determination of Low-Strain Interfaces Via Geometric Matching. *Phys. Rev. B* **2017**, *96,* 085306.
(58) Wang, Z. L.; Chen, Q.; Wang, J. L. Electronic Structure of Twisted Bilayers of Graphene/MoS2 and MoS2/MoS2. *J. Phys. Chem. C* **2015**, *119,* 4752-4758.
(59) Matsushita, Y.; Nishi, H.; Iwata, J.; Kosugi, T.; Oshiyama, A. Unfolding Energy Spectra of Double-Periodicity Two-Dimensional Systems: Twisted Bilayer Graphene and MoS2 on Graphene. *Phy Rev Mater* **2018**, *2,* 010801.
(60) Zhang, H.; Zhang, Y. N.; Liu, H.; Liu, L. M. Novel Heterostructures by Stacking Layered Molybdenum Disulfides and Nitrides for Solar Energy Conversion. *J Mater Chem A* **2014**, *2,* 15389-15395.
(61) Xia, C. X.; Du, J.; Xiong, W. Q.; Jia, Y.; Wei, Z. M.; Li, J. B. A Type-Ii GeSe/SnS Heterobilayer with a Suitable Direct Gap, Superior Optical Absorption and Broad Spectrum for Photovoltaic Applications. *J Mater Chem A* **2017**, *5,* 13400-13410.
(62) Hu, W.; Li, Z. Y.; Yang, J. L. Electronic and Optical Properties of Graphene and Graphitic ZnO Nanocomposite Structures. *J. Chem. Phys.* **2013**, *138,* 124706.
(63) Yu, Y. J.; Zhao, Y.; Ryu, S.; Brus, L. E.; Kim, K. S.; Kim, P. Tuning the Graphene Work Function by Electric Field Effect. *Nano Lett.* **2009**, *9,* 3430-3434.
(64) Wehling, T. O.; Novoselov, K. S.; Morozov, S. V.; Vdovin, E. E.; Katsnelson, M. I.; Geim, A. K.; Lichtenstein, A. I. Molecular Doping of Graphene. *Nano Lett.* **2008**, *8,* 173-177.
(65) Wang, L.; Meric, I.; Huang, P. Y.; Gao, Q.; Gao, Y.; Tran, H.; Taniguchi, T.; Watanabe, K.; Campos, L. M.; Muller, D. A.; Guo, J.; Kim, P.; Hone, J.; Shepard, K. L.; Dean, C. R. One-Dimensional Electrical Contact to a Two-Dimensional Material. *Science* **2013**, *342,* 614-617.
(66) Efetov, D. K.; Kim, P. Controlling Electron-Phonon Interactions in Graphene at Ultrahigh Carrier Densities. *Phys. Rev. Lett.* **2010**, *105,* 256805.
(67) Das, A.; Pisana, S.; Chakraborty, B.; Piscanec, S.; Saha, S. K.; Waghmare, U. V.; Novoselov, K. S.; Krishnamurthy, H. R.; Geim, A. K.; Ferrari, A. C.; Sood, A. K. Monitoring Dopants by Raman Scattering in an Electrochemically Top-Gated Graphene Transistor. *Nat. Nanotechnol.* **2008**, *3,* 210-215.
(68) Deng, S.; Li, L. J.; Zhang, Y. Strain Modulated Electronic, Mechanical, and Optical Properties of the Monolayer PdS2, PdSe2, and PtSe2 for Tunable Devices. *ACS Appl. Nano*

1
2
3 *Mater.* **2018**, *1,* 1932-1939.
4
5
6
7 Graphical abstract
8
9
10

Graphene/MoXY Heterostructures Adjusted by Interlayer Distance, External Electric Field and Strain for Tunable Devices

Shuo Deng[†‡], Lijie Li[*‡] and Paul Rees[*‡]
[†]Wuhan University of Technology, Wuhan 430070, China
[‡]College of Engineering, Swansea University, Swansea SA1 8EN, UK
[*]Emails: L.Li@swansea.ac.uk; P.Rees@swansea.ac.uk

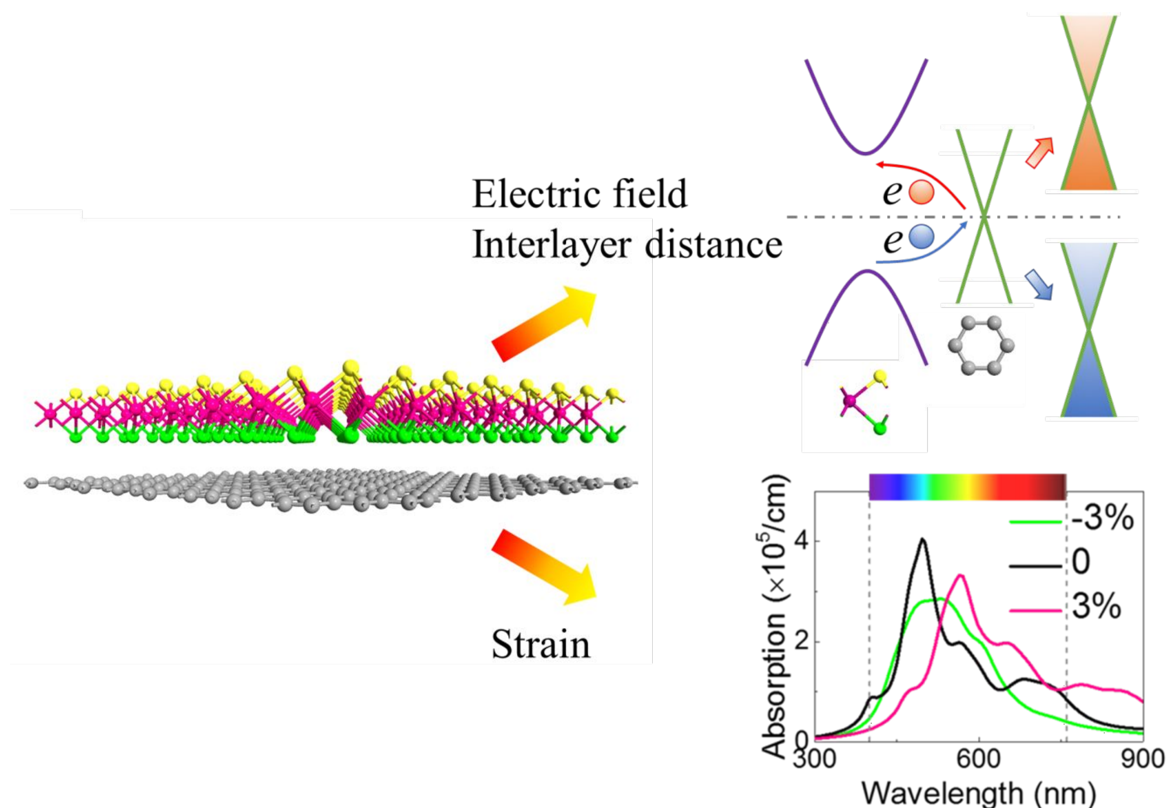

11 12 13 14 15 16 17 18 19 20 21 22 23 24 25 26 27 28 29 30 31 32 33 34 35 36 37 38 39 40 41 42 43 44 45 46 47 48 49 50 51 52 53 54 55 56 57 58 59 60